H-MODE PLASMAS AT VERY LOW ASPECT RATIO ON THE PEGASUS TOROIDAL EXPERIMENT

by

K.E. THOME, M.W. BONGARD, J.L. BARR, G.M. BODNER, M.G. BURKE, R.J. FONCK, D.M. KRIETE, J.M. PERRY, J.A. REUSCH and D.J. SCHLOSSBERG

30 SEPTEMBER 2016

*This is an author-prepared accepted manuscript of K.E. Thome et al., Nucl. Fusion **57**, 022018 (2017), DOI: 10.1088/0029-5515/57/2/022018.*

ACKNOWLEDGMENT

This material is based upon work supported by the U.S. Department of Energy, Office of Science, Office of Fusion Energy Sciences, under Award Number DE-FG02-96ER54375.

DISCLAIMER

H-mode plasmas at very low aspect ratio on the Pegasus Toroidal Experiment

K.E. Thome[a], M.W. Bongard, J.L. Barr, G.M. Bodner, M.G. Burke, R.J. Fonck, D.M. Kriete, J.M. Perry, J.A. Reusch and D.J. Schlossberg
Department of Engineering Physics, University of Wisconsin-Madison, 1500 Engineering Drive, Madison, WI 53706, USA

E-mail: thomek@fusion.gat.com

Abstract. H-mode is obtained at $A \sim 1.2$ in the Pegasus Toroidal Experiment via Ohmic heating, high-field-side fueling, and low edge recycling in both limited and diverted magnetic topologies. These H-mode plasmas show the formation of edge current and pressure pedestals and a doubling of the energy confinement time to $H_{98y,2} \sim 1$. The L-H power threshold P_{LH} increases with density, and there is no P_{LH} minimum observed in the attainable density space. The power threshold is equivalent in limited and diverted plasmas, consistent with the FM^3 model. However, the measured P_{LH} is $\sim 15\times$ higher than that predicted by conventional International Tokamak Physics Activity (ITPA) scalings, and P_{LH} / P_{ITPA08} increases as $A \to 1$. Small ELMs are present at low input power $P_{IN} \sim P_{LH}$, with toroidal mode number $n \leq 4$. At $P_{IN} >> P_{LH}$, they transition to large ELMs with intermediate $5 < n < 15$. The dominant-n component of a large ELM grows exponentially, while other components evolve nonlinearly and can damp prior to the crash. Direct measurements of the current profile in the pedestal region show that both ELM types exhibit a generation of a current-hole, followed by a pedestal recovery. Large ELMs are shown to further expel a current-carrying filament. Small ELM suppression via injection of low levels of helical current into the edge plasma region is also indicated.

Keywords: H-mode, spherical tokamaks, equilibrium reconstructions, energy confinement, ELM, ELM dynamics

1. Introduction

The H-mode operating regime [1] is the planned operating regime of ITER [2] and other burning plasma tokamak devices due to its significantly improved energy and particle confinement. It is characterized by a spontaneous, self-organized, and rapid reduction in edge turbulence and transport when sufficient input power is supplied to the plasma. While favorable for core confinement and overall fusion performance,

[a] Present address: Oak Ridge Associated Universities, Oak Ridge, Tennessee, 37831, USA.

the H-mode edge transport barrier also leads to the generation of steep gradients in equilibrium current and pressure profiles at the plasma boundary that can drive transient edge localized mode (ELM) instabilities [3].

Empirical expressions are regularly utilized to describe properties of H-mode plasmas, such as: the energy confinement time τ_e [2]; the low-to-high (L-H) power threshold P_{LH} [4]; and types of ELMs. Creating predictive, experimentally validated models of the dynamic process of the L-H transition remains an active area of research [5−7]. This is motivated in part to ensure that auxiliary heating systems are suitably sized for H-mode access in ITER and other next-step devices. Also, in these facilities ELM-induced heat loads will damage in-vessel material components. Improved understanding of ELMs is needed to develop appropriate mitigation or avoidance techniques in tokamak-based reactors [8].

Empirical expressions for H-mode properties can provide insight but are limited in their scope. For example, the 2008 International Tokamak Physics Activity (ITPA08) P_{LH} scaling [4] was constructed from high aspect ratio tokamaks ($A > 2.5$) operating in a favourable single null magnetic configuration that minimizes P_{LH}, in which the ion ∇B drift is directed towards the active X-point. Extrapolation to configurations or scales outside the bounds of available data may yield inaccurate predictions. Therefore, H-mode studies that expand the tested operating space can provide additional physics information. This knowledge can be used to improve the accuracy of these empirical expressions and, more importantly, assist in the development of appropriate first-principles physics models.

Studies at low toroidal aspect ratio A in the National Spherical Torus eXperiment (NSTX) [9, 10] and Mega Amp Spherical Tokamak (MAST) [11] spherical tokamaks (STs) have shown changes in H-mode access [4, 9, 12−13], ELM characteristics [14−16], and macroscopic equilibrium and stability characteristics [17] with respect to high-A machines. They found that more input power is required to access H-mode than predicted by conventional scalings [4, 18], including the recent ITPA08 scaling. Application of high-field-side (HFS) neutral fueling is usually required to reliably access H-mode, sometimes at reduced P_{LH} [19, 20], emphasizing the importance of neutral particle management in STs. STs also differ with respect to the optimum magnetic configuration for H-mode access. The lowest P_{LH} is achieved in the connected double null topology, in which the X-points lie on the same magnetic flux surface to within an ion gyroradius. In this geometry, the power threshold is $\sim 2\times$ lower than in the single null diverted topology, which gives the lowest P_{LH} at high A [13]. The low field and strong

shaping intrinsic to STs can result in changes to ELM peeling-ballooning stability space [21] with respect to high-A tokamaks. In particular, peeling mode drive $\propto J_{edge}/B_T$ [22−24] is emphasized at low aspect ratio. This can affect measurable ELM structures. For example, on NSTX measured magnetic ELM toroidal mode numbers have systematically lower n than observed on high-A devices [24].

H-mode access has recently been extended to very low aspect ratio ($A\sim1.2$) through experiments conducted on the Pegasus Toroidal Experiment [25]. This paper provides additional details of these first measurements [26]. It describes supporting equilibrium and confinement analyses and provides new information regarding ELMs and their nonlinear dynamics. Section 2 discusses the experimental techniques by which H-mode plasmas are achieved at $A\sim1.2$ and compares their properties to L-mode discharges at this aspect ratio. Energy confinement properties and edge pedestal measurements are provided in section 3. Section 4 details experiments conducted to characterize the L-H power threshold. ELM characteristics and their nonlinear dynamics are discussed in section 5. Concluding remarks and preliminary observations with respect to H-mode and local helicity injection (LHI) [27] are provided in section 6.

2. H-mode access at low aspect ratio

An advantage of tokamak operations at low aspect ratio is the low toroidal field B_T required to stably sustain a given plasma current I_p [17]. This leads to a correspondingly low anticipated L-H power threshold with respect to empirical P_{LH} scalings. For example, the ITPA08 formulation

$$P_{ITPA08}=0.0488n_{20}^{0.717}B_T^{0.803}S^{0.941} \tag{1}$$

gives a prediction for P_{LH} in MW as a function of line-average density in 10^{20} m^{-3}, toroidal field in T, and plasma surface area S in m^2 for deuterium plasmas in the favourable single null diverted topology [4]. An earlier ITPA04 scaling relation proposed explicit aspect ratio dependences with the relation

$$P_{ITPA04}=0.072\left|B_{out}\right|^{0.7}n_{20}^{0.7}S^{0.9}\left(\frac{Z_{eff}}{2}\right)^{0.7}\left[\frac{0.1A}{1-\sqrt{2/\left(1+A\right)}}\right]^{\gamma}, \tag{2}$$

where $B_{out}^2=B_{Tout}^2+B_{pout}^2$ is the magnetic field at the outboard midplane with $B_{Tout}=B_TA/(A+1)$, $B_{pout}=\left(\mu_0I_p/2\pi a\right)\times\left(1+A^{-1}\right)$, a is the minor radius, Z_{eff} the effective charge number, and

$\gamma = 0.5 \pm 0.5$ quantifies the nonlinear aspect ratio-dependence of the scaling [12]. Both scalings have a near-linear B_T dependence, leading to low P_{LH} as A is reduced.

Thus, these scalings predict very low estimates for P_{LH} at the ultralow A of Pegasus. Figure 1 shows the predicted P_{LH} for representative Pegasus plasma parameters (major radius $R_0 = 0.35$ m, $A = 1.19$, $B_T = 0.165$ T, elongation $\kappa = 2$, and Greenwald fraction $n_G = 0.5$) using the ITPA08 and ITPA04 scalings as a function of I_p. The shaded region for the ITPA04 scaling indicates bounds for P_{LH} given $\gamma = 0 - 1$. For comparison, the input power for Ohmically-heated plasmas in Pegasus is plotted for a range of plasma currents $I_p \approx 50 - 150$ kA. The time evolution of these relatively short pulse plasmas results in $P_{LH} \sim 0.7 P_{OH}$. Thus, the experimentally realized P_{LH} exceeds the predictions of the ITPA08 scaling by $7 - 15\times$.

Consistent with H-mode access on other tokamaks, H-mode access at $A \sim 1.2$ requires careful management of neutral particles. Low edge recycling via titanium gettering and HFS fueling are used to facilitate L-H transitions. Two such fueling systems are available on the Pegasus centerstack; they inject gas at $Z = \pm 0.3$ m. The systems each consist of a PV-10 piezoelectric valve located outside of the vessel and a ~ 1.7 m long capillary tube.

H-mode has been accessed in two magnetic topologies to date. Figure 2 depicts representative fast visible camera images of limited L-mode (a), limited H-mode (b), and upper single null diverted H-mode plasmas (c) recorded with a Phantom v12 camera using a fisheye lens and an exposure time of ~30 μs. The location of HFS fueling is reflected by the bright spot(s) on the centerstack. Such fast visible camera images of Pegasus plasmas are often used to distinguish between the L-mode and H-mode operating regimes via the transition from a turbulent L-mode edge (figure 2(a)) to a quiescent H-mode edge (figure 2(b)) with reduced visible emissions. This transition occurs on fast imaging in $\lesssim 1$ ms.

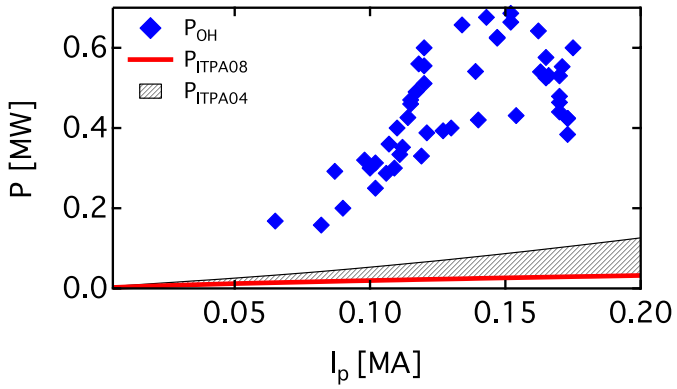

Figure 1. Pegasus H-mode power requirements given by the ITPA08 (solid red) and ITPA04 (black shaded) scalings compared to experimental Ohmic input power (blue diamonds).

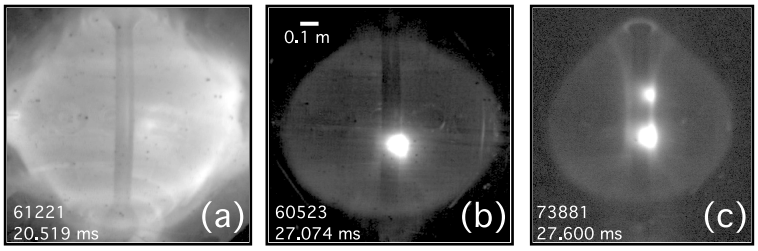

Figure 2. Fast visible camera images of limited L-mode (a), limited H-mode (b), and diverted H-mode (c) plasmas. Figures (a) and (b) reproduced with permission from [26]. Copyright 2016 American Physical Society.

Figure 3 compares waveforms from limited Ohmic L- and H-mode discharges with matched loop voltage and equilibrium field programming. They achieved comparable $I_p \sim 0.1$ MA (figure 3(a)) and shape. However, these discharges differed by fueling method. The L-mode plasma was fueled exclusively from the LFS while the H-mode plasma was fueled exclusively from the HFS after its bifurcation near 20 ms. The use of HFS fueling reduces the outboard neutral pressure measured by a fast ion gauge by $\sim 2\times$ compared to the LFS fueling case (figure 3(b)). However, the line-averaged electron density $\bar{n}_e$ (figure 3(c)) only differs by ~30%. The L-H transition is identified by the appearance of the sharp edge on the fast framing camera. It is accompanied by a drop in the midplane D_α emissions, observed tangentially, (figure 3(d)) and by the divergence of the diamagnetic loop toroidal flux Φ_D from $\Phi_D \sim 1$ mWb (L-mode) to $\Phi_D > 2$ mWb (H-mode) (figure 3(e)), which occurs on the order of an energy confinement time. Magnetic equilibrium reconstructions show that the observed increase in paramagnetism in H-mode reflects increases in both stored energy and internal inductance, with $\ell_i \sim 0.3$ in the L-phase and ~ 0.4 in

the H-phase at the end of the discharge. An ELM event is illustrated by the spike in the H-mode D_α emissions (figure 3(d)).

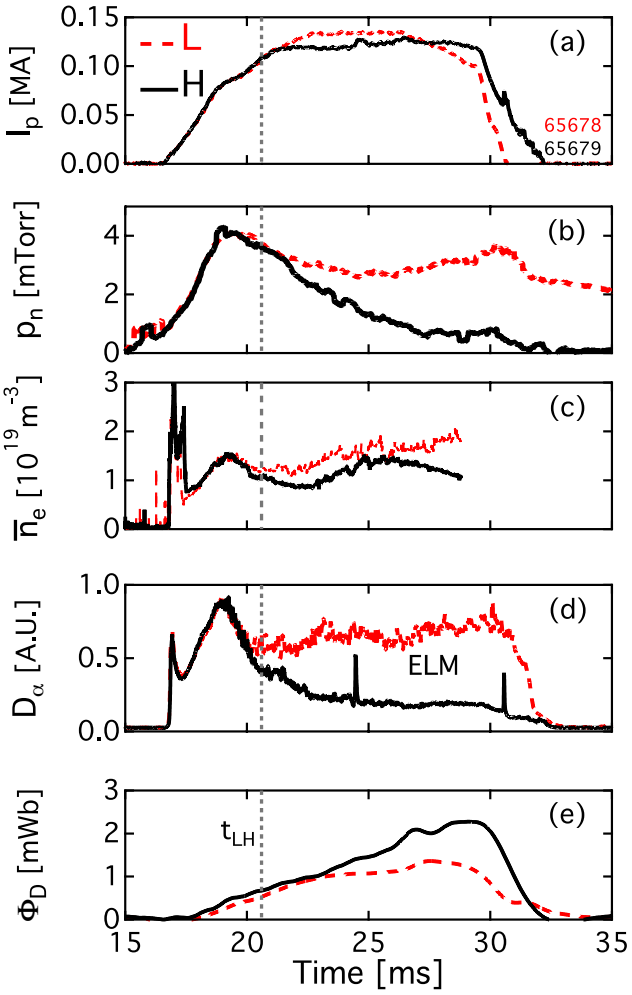

Figure 3. I_p (a), outboard neutral pressure (b), line-averaged density (c), D_α emission (d), and diamagnetic loop flux Φ_D (e) of similar limited H-mode (solid black) and L-mode (dashed red) discharges. Dashed vertical line indicates the nominal L-H transition time. Figures (a), (d), and (e) reproduced with permission from [26]. Copyright 2016 American Physical Society.

Pegasus H-mode plasmas have increased core intrinsic toroidal rotation compared to L-mode plasmas. Passive ion spectroscopy [28] was used to measure the intrinsic impurity toroidal rotation and impurity temperatures for the discharges shown in figure 3. The rotation was determined by measuring the Doppler shift of an OV impurity line [$\lambda = 278.101$ nm] along midplane viewing chords with varied tangency radii with respect to a radial sight line. Figure 4 shows chordally-integrated rotation profiles for the L- and H-

mode discharges, averaged over 27−28 ms as a function of the radial-like coordinate $\sqrt{\psi_N}$ derived from KFIT equilibrium reconstructions [23, 29]. The L-mode discharge has negligible toroidal rotation for $\sqrt{\psi_N} < 0.6$. Measurement of the rotation at higher radii was not possible during this L-phase, as OV impurity excitation was not observed. In contrast, the H-mode core plasma is rotating strongly in the counter-current direction with a speed of 10 km s^{-1}. This observation of increased intrinsic toroidal rotation in the counter-current direction following an H-mode transition may be unique. Generally, increased intrinsic rotation is observed in the co-current direction after an H-mode transition [30]. Previously, the direction of intrinsic rotation has been observed to change with turbulence type [31]. This apparent contrast with other experiments merits future investigation of the relationship between turbulence and intrinsic rotation observed in low-field and low-density H-mode plasmas on Pegasus.

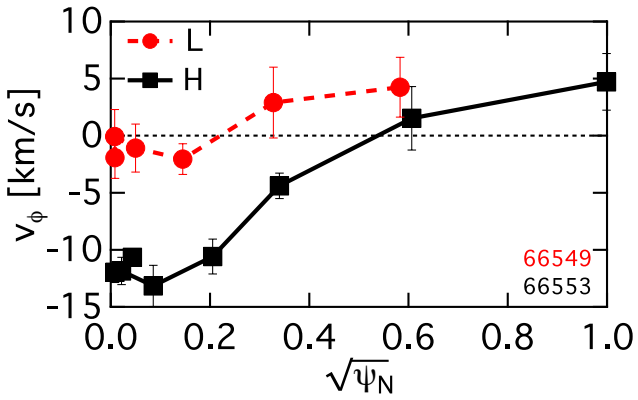

Figure 4. OV intrinsic toroidal rotation profiles for figure 3 discharges.

Similarly, figure 5(a) compares OV and CV impurity temperatures along a chord with $R_{\tan} \approx 0.34$ m, situated near the plasma geometric axis of $R_0 \approx 0.32$ m. This centrally-weighted $T_{i,z}(r \sim 0)$ increases throughout both discharges (figure 5(a)). However, following the L-H transition, the H-mode scenarios have a higher ion heating rate, with $T_{i,z}(r \sim 0) \sim 40$ eV and ~ 60 eV at the end of the L-mode and H-mode discharges, respectively.

These H-mode plasmas appear to have higher core electron temperatures T_e compared to their L-mode counterparts. Core-localized CV emission ($\lambda = 227.091$ nm, ionization potential $E_i = 392$ eV) is only

observed in H-mode, implying these H-mode plasmas have higher core T_e than in L-mode. Figure 5(b) shows the CV intensity evolution for several sight lines ranging from the core region at $R_{\tan} \approx 0.34$ m to a near-edge chord at $R_{\tan} \approx 0.51$ m in the H-mode discharge. The CV emission becomes centrally peaked over time, suggesting that $T_e(R,t)$ is also centrally peaked. At the end of the discharge, the impurity emissions have not equilibrated, indicating that transport equilibrium has not yet been achieved.

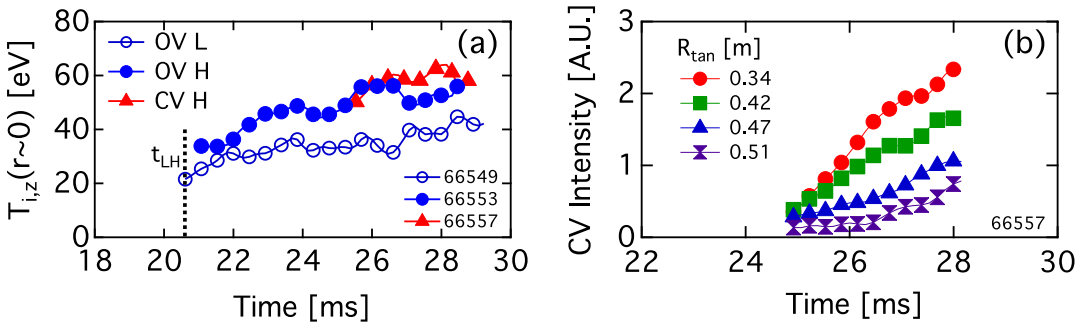

Figure 5. Impurity $T_{i,z}(r \sim 0)$ (a) and tangential H-mode CV intensity (b) for discharges of figure 3. Measurement uncertainties are smaller than the marker size.

Preliminary indications of the core electron temperature $T_e(0)$ were obtained using a Thomson scattering system [32] with a spectrometer optimized to resolve $T_e \lesssim 150$ eV. Scattered spectra were obtained in limited L-mode and H-mode discharges at 29 ms, a period with comparable $I_p \sim 100$ kA (figure 6(a)). The line-averaged densities were $\bar{n}_e = 1.8 \times 10^{19}$ m^{-3} and $\bar{n}_e = 1.1 \times 10^{19}$ m^{-3} in the L- and H-mode discharges, respectively. Thomson scattering spectra centered about the 532 nm Nd:YAG laser wavelength are shown for the L- and H-mode discharges in figures 6(b) and (c), respectively. The L-mode $T_e(0)$ was 151 ± 20 eV. Increased spectral broadening is observed in the H-mode spectrum, combined with an amplitude decrease of $\sim 3\times$. The H-mode $T_e(0)$ can be reasonably bounded above $T_e(0) > 200$ eV by comparing the total scattering intensity between the two confinement modes to the analytic, relativistic Thomson scattering model by Selden [33].

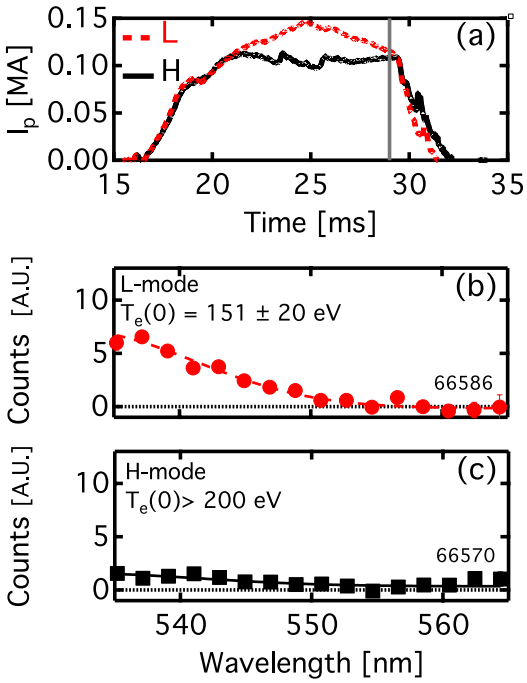

Figure 6. Preliminary Thomson scattering measurements. I_p (a) with line showing measurement time, L-mode $T_e(0)$ (b), H-mode $T_e(0)$ (c).

3. Energy confinement properties and pedestal characteristics

3.1 Energy confinement characterization

The energy confinement time τ_e was determined for several Pegasus discharges by performing time-evolving equilibrium reconstructions with the KFIT code [23, 29], constrained by external magnetics and a diamagnetic loop. These include Ohmic limited, diverted, L-mode, and H-mode plasmas, as well as Ohmic sustainment phases following LHI non-inductive startup [27]. The energy confinement time was determined at the end of the high current phase of the discharge in order to allow it as much time as possible to evolve within the available pulse length. In order to account for evolving magnetic and kinetic energy terms, τ_e was calculated with the expression

$$\tau_e = \frac{W_K}{P_{IN}} = \frac{W_K}{I_p V_{loop} - \frac{dW_K}{dt} - \frac{dW_M}{dt} - P_{RAD}}, \tag{3}$$

where W_K is the kinetic energy, V_{loop} is the applied loop voltage, W_M is the magnetic energy, and P_{RAD} is the radiated power [34]. Radiated power was neglected in this analysis, based on prior work that

showed it is generally negligible [35]. Due to the short pulse length, the H-phase evolves only through a few τ_e at most. The plasma equilibrium tends to evolve towards higher τ_e as W_K increases as the pulse time increases. Hence, the τ_e reported here generally represent lower bounds.

Figure 7 illustrates equilibrium results from this analysis for an $I_p \sim 90$ kA, upper single null diverted discharge with an L-H transition. Equilibrium flux contours and global parameters for time points prior to and following the L-H transition are provided in figures 7(a) and (b), respectively. The time evolutions of the plasma kinetic and magnetic energy components are shown in figure 7(c). During the L-mode phase, W_K and W_M are both constant at ~ 200 J. A clear bifurcation in $W_K(t)$ and $W_M(t)$ accompanies the L-H transition near 25.5 ms. Afterward, both terms increase compared to their L-mode values. Ultimately, the kinetic energy increases by $\sim 3\times$ to 600 J at the end of the Ohmic pulse. Note, however, that the stored energy components are monotonically increasing throughout the available pulse length and therefore are not in transport equilibrium. The dashed line in the figure indicates the predicted trajectory for $W_K(t)$ assuming an instantaneous transition in the L- to H-mode confinement time at the specified transition time.

Table 1 summarizes the results from these confinement analyses. In the data set, τ_e varied from ~1–7 ms. Since the properties of these plasmas differed, comparisons of L- and H-mode energy confinement is best described using a normalization to the IPB98(y,2) confinement time scaling via the $H_{98y,2}$ factor; *i.e.* $H_{98y,2} = \tau_e / \tau_{e98y,2}$ [2]. The average $H_{98y,2}$ for L-mode plasmas in this data set is found to be 0.55 ± 0.2. Similarly, the average $H_{98y,2}$ of limited H-modes is 0.85 ± 0.2. Including both limited and diverted H-modes yields an average H-mode $H_{98y,2}$ of 1.0 ± 0.2. Thus, the energy confinement improves by approximately a factor of two in H-mode plasmas compared to L-mode plasmas.

The single diverted H-mode scenario present in this data set indicates a higher $H_{98y,2} \sim 1.5$ with respect to its limited counterparts. However, higher uncertainty in its determination is expected due to more strongly evolving energy components in the τ_e determination. These results may hint at a net improvement in confinement in the diverted configuration but additional data is required to substantiate

this observation.

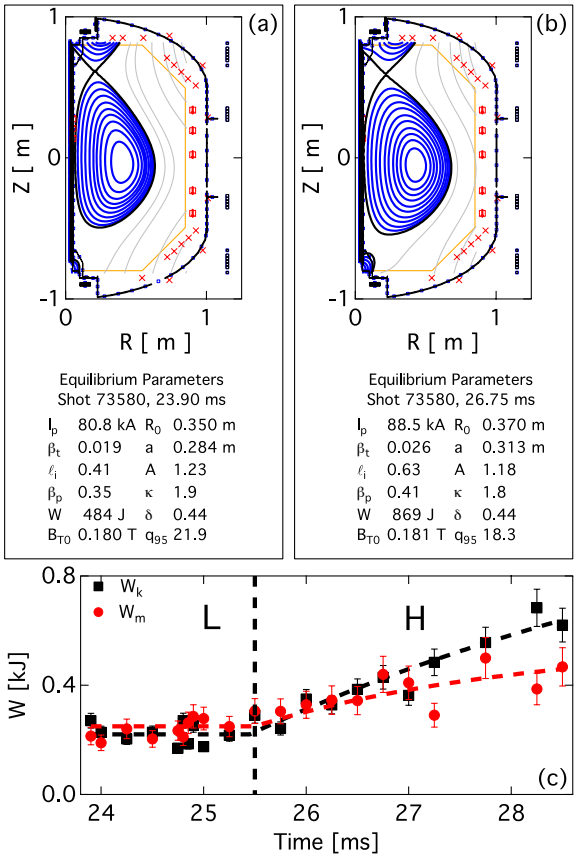

Figure 7. Sample equilibrium reconstructions from confinement analysis. L-mode (a), H-mode time points (b); stored energy component temporal evolution (c).

Table 1. Energy confinement parameters for reconstructed discharges.

SN	Type	Phase	I_p (kA)	P_{IN} (kW)	$\bar{n}_e$ (10^{19} m^{-3})	τ_e (ms)	$H_{98y,2}$
65673	Limiter	H	120	250	1.3	2.1	0.8
65678	Limiter	L	120	590	1.7	1.2	0.7
66221	Limiter (+LHI)	H	170	210	1.0	4.3	1.2
67197	Limiter	H	130	280	1.4	1.4	0.5
73580	Diverted	L	86	280	1.2	0.8	0.4
73580	Diverted	H	92	80	0.6	6.7	1.5

3.2 Edge pedestal characterization

Operation at $A \sim 1.2$ and $B_T \sim 0.15$ T in Pegasus produces H-mode conditions with modest edge electron temperatures. This allows direct pedestal diagnostic access using magnetic and electrostatic probes with high spatiotemporal resolution. They have been used here to measure pedestal formation in the edge current density and pressure, respectively.

Edge current profiles are measured using a radially scanning, sixteen channel array of radially separated Hall effect sensors ($\delta R \sim 0.75$ cm) that are oriented to measure $B_Z(R,t)$ [36]. The Hall probe was positioned at $Z = 0$ cm to sample the edge poloidal field directly (*i.e.* $B_p = B_Z$). Such measurements are directly related to the local toroidal current density $J_\phi(R,t)$ via Ampère's Law. In a conventional cylindrical coordinate system,

$$\mu_0 J_\phi = \left(\nabla \times \mathbf{B}\right)_\phi = \frac{\partial B_R}{\partial Z} - \frac{\partial B_Z}{\partial R} \tag{4}$$

with the local B_R term eliminated in practice by virtue of the sensor measurement locations [26], and its derivative estimated via assumptions of local Grad-Shafranov equilibrium in conjunction with available $B_Z(R)$ data [22,23,37].

An edge current pedestal is measured following the L-H transition. Figure 8 shows the resulting direct J_ϕ profiles for the L- mode and H-mode discharges depicted in figure 3 determined at 28 ms, where $I_p \sim 120$ kA. The nominal pedestal width contracts to ~ 2 cm in H-mode, from approximately double that in L-mode.

The simultaneous observation of an edge current pedestal and increased ℓ_i in H-mode plasmas compared to L-mode plasmas is linked to low-A geometric effects. At $A \sim 1$, the radial distribution of toroidal current is highly poloidally asymmetric when ℓ_i is very low, with the high-field-side J_ϕ two to four times higher than on the low-field-side for Pegasus L-mode plasmas. This in-out current profile asymmetry decreases substantially as ℓ_i increases due to the strong toroidicity of the ST configuration.

This effect is indicated using model equilibria generated for the Pegasus geometry. Figure 9 shows such sample midplane $J_\phi(R)$ for discharges with comparable shape, current, and W_K but varied ℓ_i.

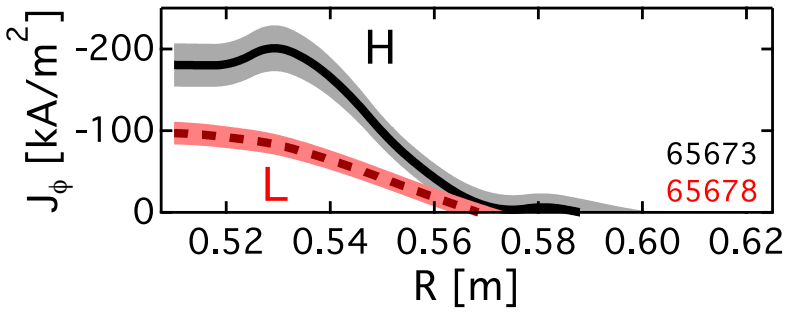

Figure 8. Current profiles for H-mode (solid black) and L-mode (red dashed) discharges. Reproduced with permission from [26]. Copyright 2016 American Physical Society.

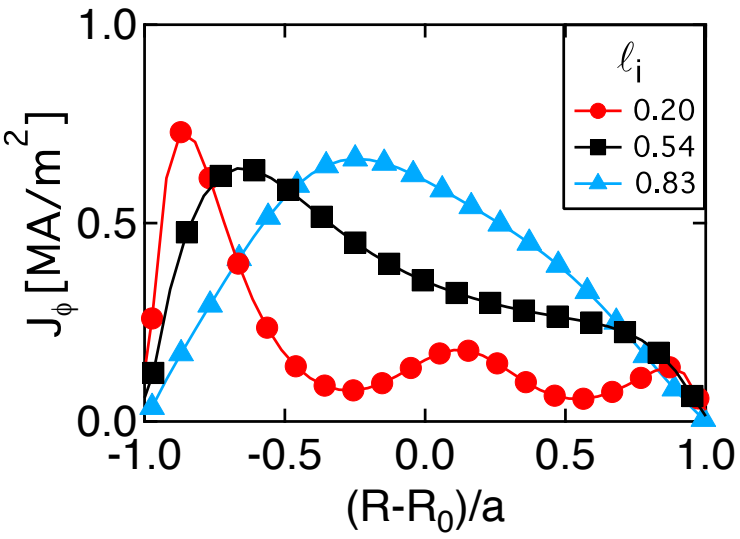

Figure 9. Model current profiles at $A \sim 1.2$ for various ℓ_i.

Multi-shot radial Langmuir probe scans of L- and H-mode discharges indicate a pressure pedestal forms following the L-H transition. Initial measurements of edge pressure profiles were obtained using multi-shot radial scans of an insertable triple Langmuir probe. This approach is facilitated by good shot-to-shot reproducibility of discharge I_p and shape. However, the measurements were complicated by the presence of large scale, low-m, $n=1$ internal tearing mode activity commonly observed in Ohmic Pegasus discharges [38]. This mode caused the edge to move several centimeters during its ~100 μs MHD cycle.

Figures 10(a) and (b) show two fast camera images taken at different phases of the MHD measured with a Mirnov coil (figure 10(c)). The Langmuir probe location is fixed and is visible at the left-hand side of the plasma. The plasma edge expands and contracts in phase with the low-n MHD activity. The local edge pressure measurements (figure 10(d)) also oscillate at the MHD frequency.

To account for this edge oscillation, the local pressure measurements for each radial location were averaged over temporal periods corresponding to the lowermost and uppermost extrema of the recorded phases in a three-millisecond period at the end of the discharge. This conditional averaging produces $p(R)$ profiles with clear edge/scrapeoff layer boundaries that are displaced by several cm, consistent with the observed edge displacement on visible imaging.

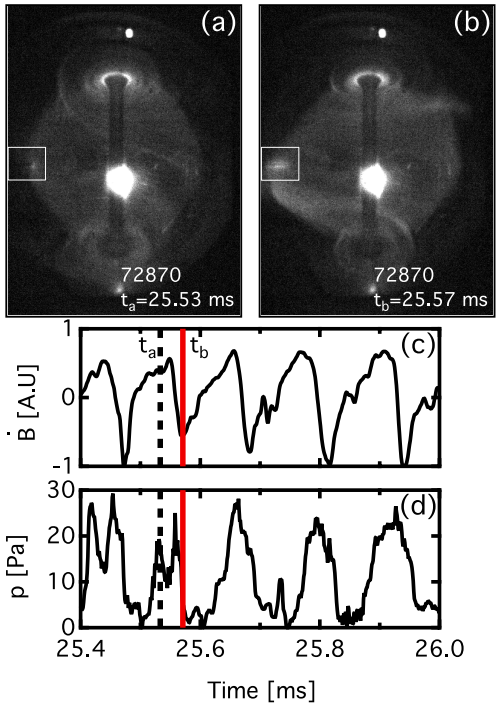

Figure 10. Fast camera images illustrating plasma edge fluctuation inwards (a) and outwards (b) at fast time scales over Langmuir probe (white box outline); MHD-modulated Mirnov signal (c) and electron pressure (d) waveforms.

The high-radial-displacement and low-radial-displacement pressure profiles were combined by shifting their radius relative to the plasma edge position and removing their DC offsets. The resulting ensemble profiles from this analysis are shown in figure 11, along with representative plasma currents for these cases. The L-mode data show a linear increase in pressure with distance from the boundary. In contrast, the H-mode data exhibit a sharp rise inward from the boundary that is better represented by a conventional modified hyperbolic tangent profile [39].

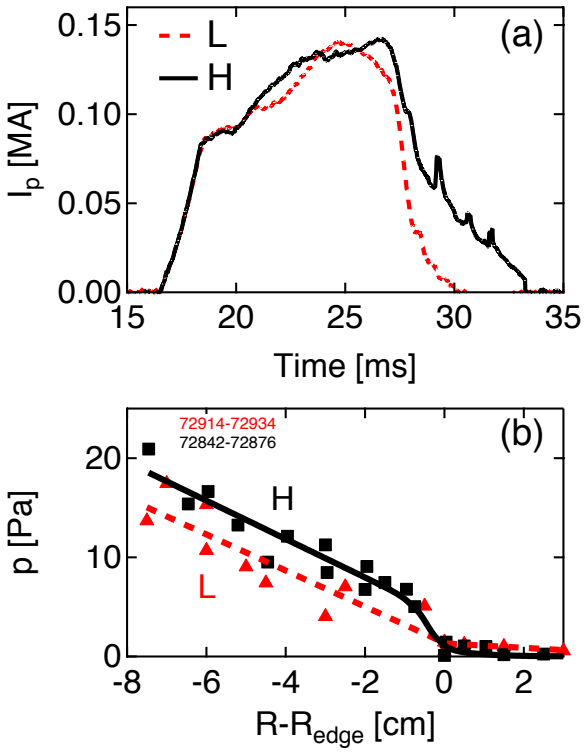

Figure 11. Baseline $I_p(t)$ (a) and ensemble-averaged pressure profiles (b) for L-mode (dashed, triangles) and H-mode (solid, squares) discharges. Figure (b) reproduced with permission from [26]. Copyright 2016 American Physical Society.

4. L-H power threshold

This section reports supporting details of the first experiments to characterize the L-H power threshold at $A \sim 1.2$ as a function of Ohmic input power $P_{OH} = I_p V_{loop}$, magnetic topology, and density [26]. Variations in P_{OH} are sufficient to explore access to H-mode, as shown in figure 12. It shows a set of varied $P_{OH} = 0.2 - 0.6$ MW induced by perturbative V_{loop} steps at 20 ms for a series of discharges that transitioned to H-mode with ~ 300 kW of input power. L-H transitions are observable by the bifurcation in diamagnetic flux (figure 12(b)), plasma edge sharpening in fast visible imaging (figure 2), sharp drop in D_α emissions (*e.g.* figure 3(d)), and/or through time-evolving equilibrium reconstructions (figure 7(c)).

The power threshold was measured in two magnetic geometries. Figure 13 depicts equilibrium reconstructions of representative inner-wall limited (figure 13(a)) and favourable upper single null diverted (figure 13(b)) discharges in these experiments. This diverted geometry offers direct comparisons

to the ITPA08 empirical power threshold scalings but may not provide minimum P_{LH} values at $A \sim 1$.

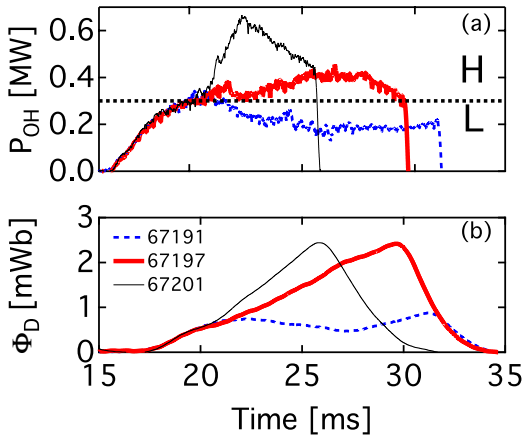

Figure 12. Power threshold experiments on Pegasus. Examples of varying P_{OH} (a) and the resulting Φ_D (b).

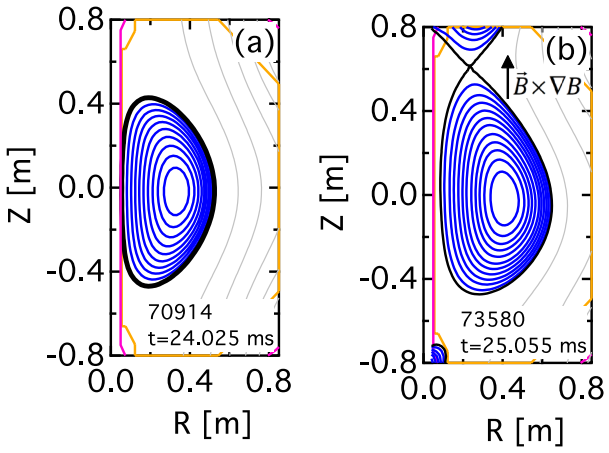

Figure 13. Equilibrium flux plots of inner-wall limited (a) and favourable upper single null diverted (b) plasmas from P_{LH} experiment.

The Ohmic input power required to access H-mode on Pegasus was determined as a function of density using a survey of over 100 limited and upper single null diverted discharges. These discharges spanned $0.05 < P_{OH} < 0.6$ MW, $\bar{n}_e = 0.5-5\times10^{19}$ m^{-3}, and $n_G = 0.1-0.8$. Figure 14 summarizes the results of this input power threshold survey for both configurations. Discharges that exhibited an L-H transition are denoted with solid symbols and plotted here at the corresponding $P_{OH}/\bar{n}_e$ values, averaged 0.25 ms over the L-H transition time. Open symbols denote similarly-averaged discharge periods in L-mode. This

allows multiple time-points with strong variations in $P_{OH}/\bar{n}_e$ to be included from a single discharge. A reduced dataset of this figure with P_{OH} normalized to the B_T and S dependencies from the ITPA08 scaling is published in [26] as figure 3.

Three salient features arise from the data sets shown in figure 14. First, within evident scatter, there is a clear separation between L- and H-mode data, indicating the existence of a power threshold. This is denoted in figure 14 by a dashed line. Second, the power threshold increases monotonically with density in this range, with no P_{LH}-minimizing density $n_e^{\min}$ observed [40]. Finally, the power threshold appears equivalent in limited and diverted topologies.

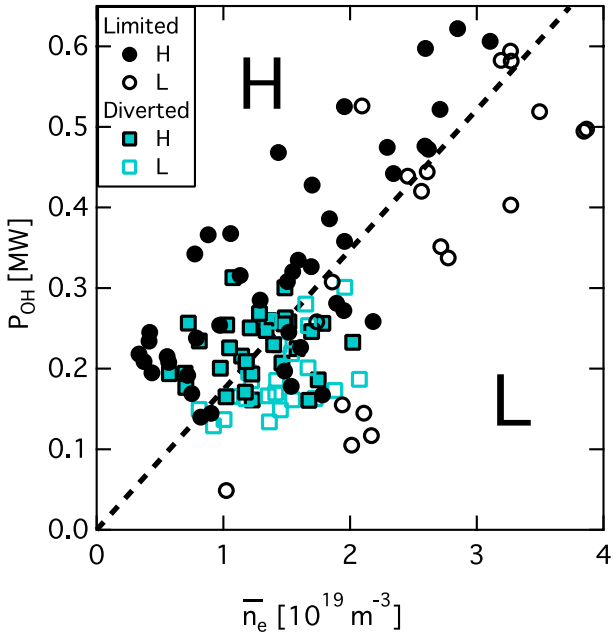

Figure 14. L-, H-mode $P_{OH}-\bar{n}_e$ operating space separated by visual trend line (dashed).

The lack of a P_{LH}-minimizing density $n_e^{\min}$ and the equivalence between limited and diverted power thresholds at $A\sim 1.2$ are consistent with the FM^3 L-H transition model [7]. For Pegasus edge parameters, $n_e^{\min}\sim 1\times 10^{18}$ m^{-3} is predicted from the FM^3 model, which was too low to access due to runaway electron production. The model also postulates that the difference in power threshold between the two magnetic topologies is due to the safety factor at the radial location of the L-H transition $q_\star$, with

$P_{LH}^{LIM} / P_{LH}^{DIV} \approx \left(q_{\star}^{LIM} / q_{\star}^{DIV} \right)^{-7/9}$. At high A, this is consistent with the higher observed P_{LH} in limited plasmas, where $P_{LH}^{LIM} / P_{LH}^{DIV} \gtrsim 2$ [41, 42]. In contrast at $A \sim 1.2$, $q_{\star}^{LIM} \approx q_{\star}^{DIV}$. This is demonstrated in figure 15 for the Pegasus magnetic configurations of figure 13. Significant magnetic shear is present in both limited and diverted configurations at $A \sim 1.2$, causing only weak variations in $q_{\star}$ between topologies. Thus, a similar power threshold is predicted by this model at very low aspect ratio, in agreement with experiment.

The power threshold value was determined for a subset of the discharges in figure 14 by performing time-evolving magnetic reconstructions to determine

$$P_{LH} = P_{IN}(t_{LH}) = P_{OH} - \frac{dW}{dt} - P_{RAD} \tag{5}$$

at times spanning the L-H transition. As in the energy confinement calculations, P_{RAD} was assumed to be negligible. The corrections from dW / dt in this analysis were $\lesssim 30$ %, with $P_{LH} \sim 0.7 P_{OH}$ typical. Thus, the power required to access H-mode on Pegasus is 200−400 kW, which is $\sim 15\times$ higher than predicted by the ITPA08 scaling [26]. If the lowest P_{LH} in a connected double null geometry ST trend applies to Pegasus, P_{LH} at $A \sim 1.2$ would still be $\sim 8\times$ higher than the ITPA08 scaling. If instead a comparison is made with the ITPA04 scaling, using the maximum $\gamma = 1$ and assuming $Z_{eff} \sim 1$ based on previous work [35], the Pegasus P_{LH} is $\sim 6\times$ higher than the ITPA04 scaling.

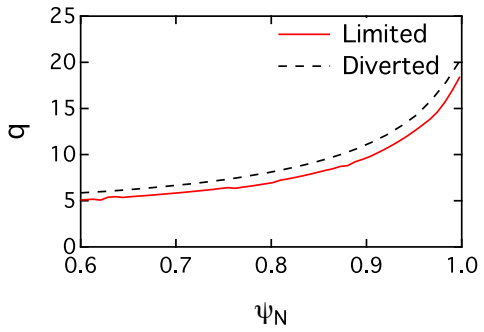

Figure 15. Edge safety factor profiles of limited and diverted discharges in figure 13.

5. Edge localized modes

ELMs are regularly observed in Pegasus H-mode plasmas. Similar to other tokamaks [43], ELMs

generate characteristic bursts of D_α emissions that are temporally correlated with the creation of propagating, field-aligned filamentary structures on fast visible imaging on Pegasus. To date, two classes of ELMs have been observed. They are distinguished here by their measured magnetic n spectra and their occurrence at different values of input power P_{IN} relative to P_{LH}, as ELM classification by their frequency/power relationship [3, 44] is not possible due to the lack of auxiliary heating. Small ELMs are present at $P_{IN} \sim P_{LH}$. As P_{IN} is increased, they transition to large ELMs. ELM virulence increases further as P_{IN} increases, potentially terminating discharges when $P_{IN} / P_{LH} \gtrsim 2$.

Fast visible camera images of these two ELM types are shown in figure 16. A small ELM (figure 16(a), contrast enhanced) generates many filaments with respect to a quiescent, inter-ELM H-mode edge (see figures 2(b) and (c)). These filaments generally produce only small edge disturbances. In contrast, the large ELM depicted in figure 16(b) is very bright and has a single dominant filament. The higher energy losses associated with these large ELMs also generate characteristic spiral heat deposition patterns on the upper and lower divertor plates.

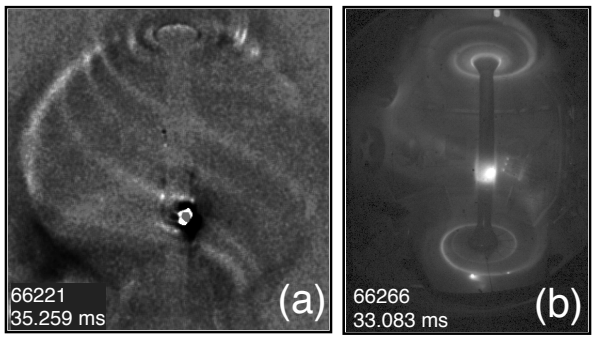

Figure 16. Fast camera images of small ((a), contrast enhanced) and large (b) ELMs.

Variations in Ohmic input power can readily affect the ELMs produced in Pegasus. Figure 17 demonstrates a discharge that transitions from the small ELM regime to the large ELM regime by increasing P_{OH}. $I_p(t)$ is shown in figure 17(a). Estimates for $P_{IN}(t)$ and $P_{LH}(t)$ are shown in figure 17(b). Here, $P_{IN}(t)$ is estimated by assuming that $dW / dt \approx (.4 \pm .1) P_{OH}$ and P_{RAD} is negligible, and the plotted $P_{LH}(t)$ is taken to be $P_{LH} \approx 15 P_{ITPA08}$. The experimental ITPA08 estimate is inferred using a fast boundary reconstruction code and interferometry measurements, and the scalar multiplier is chosen consistently with estimates from previous results [26] and those presented in section 4. D_α emissions are

shown in figure 17(c). The discharge begins in L-mode with low power and LFS fueling. As the power is increased and HFS fueling engaged, an H-mode transition occurs near 20 ms. Small ELMs appear immediately after the transition, as indicated by the small spikes in the D_α signal. Each small D_α perturbation coincides with filament bursts similar to those depicted in figure 16(a). As P_{IN} is increased, ELM generation ceases, leading to a ~ 4 ms quiescent period that is also free of low-n core tearing mode activity. This is terminated at 27.5 ms by the onset of a virulent, large ELM when $P_{IN} >> P_{LH}$. This particular high-power ELM appears to stimulate an H-L back-transition due to the large drop in I_p at the event. At lower input power, I_p is less affected and similar large ELMs do not cause back-transitions.

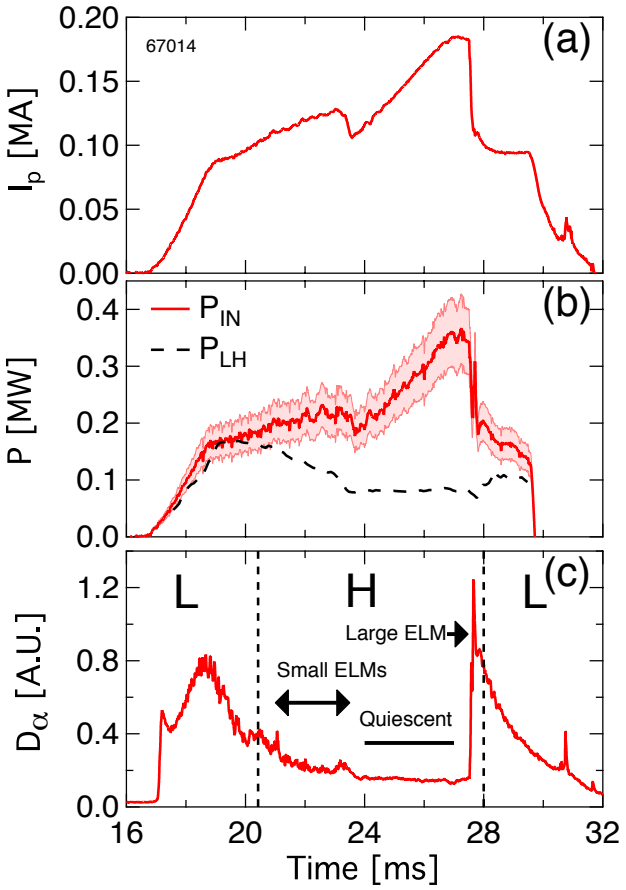

Figure 17. I_p (a), estimated P_{IN} (solid red line) and P_{LH} (dashed black line) (b), and D_α (c) waveforms for a discharge with both small and large ELMs.

Both ELM types generate observable magnetic precursors. Mode spectra are derived from cross-phase spectral analysis of a toroidal Mirnov coil array placed ~2 cm exterior to the plasma boundary [22].

Multiple n are observed during ELMs [26], consistent with the theoretical expectation of the simultaneous presence of multiple unstable peeling-ballooning modes [45−48]. Small ELMs have low $n \leq 4$, whereas large ELMs have intermediate $5 < n < 15$ present. Such mode numbers are similar to those observed in Type III and Type I ELMS, respectively, at $A \sim 1.3$ in NSTX [14]. However, the mode numbers for both large and small ELMs in Pegasus are systematically lower than those observed at high A [16, 44], presumably due to the higher peeling mode drive $\propto J_{edge} / B_T$ at low A [22,23,26].

Figure 18 shows results from spectral analysis of magnetic signals from the large ELM event in figure 17 in a 500 μs period preceding the measured D_α rise as an example. Figure 18(a) depicts the autopower spectrum of a single near-edge Mirnov coil and n identified from cross-phase analysis of multiple sensors (figure 18(b)). Multiple coherent spectral bands are present, leading to small cross-phase angle $\hat{\theta}$ uncertainty and clear identification of n from the linear slope of the measured cross phase when plotted as a function of sensor toroidal angle. Figures 18(c) through (f) show bandpass-filtered Mirnov dB_z / dt signals ((c) and (e)) and their amplitudes ((d) and (f)) calculated via the Hilbert transform. These show the temporal evolution of the dominant $n = 8$ mode and a representative sub-dominant $n = 6$ mode. The $n = 8$ mode grows continuously throughout this time period. In contrast, the $n = 6$ mode evolves nonlinearly and damps prior to the ELM crash. Such activity is observed in nonlinear simulations of ELMs [45].

The high spatiotemporal resolution of the Pegasus Hall probe and simplified diagnostic pedestal access at low A allows unique measurements of nonlinear ELM dynamics [26]. Figure 19 shows the evolution of the local edge current profile through single small (figures 19(a)−(e)) and large ELM (figures 19(f)−(j)) events. Both ELM types feature the generation of current-hole perturbations [22] that precede the ELM crash. The large ELM data demonstrates the ejection of a current-carrying filament. The generation and expulsion of such filaments due to peeling-ballooning instabilities are postulated by electromagnetic blob transport theory [48] and are observed in nonlinear simulations of ELMs [46, 47, 49]. The timescales of the two ELM events differ with the small ELM occurring over ~0.8 ms and the large ELM occurring over ~0.4 ms. The large ELM also creates a bigger disturbance in the edge current.

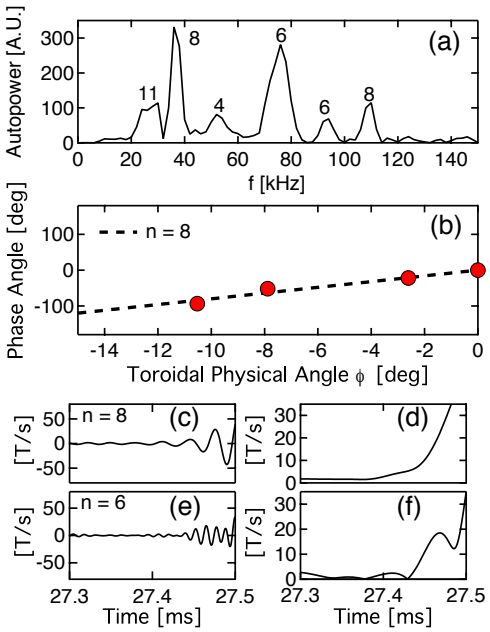

Figure 18. Magnetic spectral analysis of large ELM in figure 17: autopower spectrum and n (a); cross-phase $\hat{\theta}(\phi)$ and $n=8$ mode identification (b); $n=8$ dB_z/dt (c) and envelope function (d); $n=6$ dB_z/dt (e) and envelope function (f).

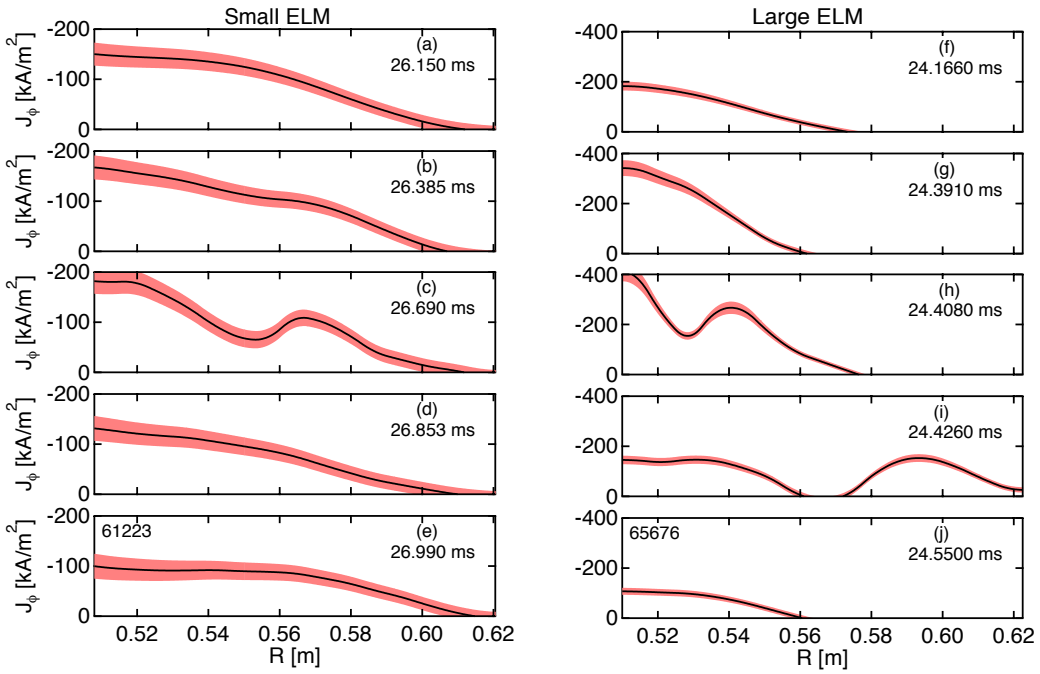

Figure 19. Edge current profile evolution through small (a)−(e) and large (f)−(j) ELMs.

6. Discussion and conclusion

This work extends observations of the H-mode confinement regime to $A \sim 1.2$. H-mode is readily accessible in a small-scale, low aspect ratio tokamak with Ohmic heating alone in both limited and diverted configurations. The characteristics of this regime are generally similar to that observed at higher A, including: the formation of a quiescent edge; formation of edge pressure and current pedestals; changes in intrinsic toroidal rotation; improved energy confinement, consistent with the IPB98(y,2) H-mode scaling; and increased heating of the electron and ion channels.

Experimental surveys of the L-H power threshold at ultralow A were conducted. A monotonically increasing power threshold with density is observed, consistent with empirical scaling relations and FM^3 model predictions. A unique low-A feature is the equivalence of the measured power threshold in limited and diverted plasmas, which is consistent with the FM^3 model. In both configurations, P_{LH} exceeds predictions of the ITPA08 and FM^3 models by $\sim 15\times$. This work confirms and extends prior measurements of P_{LH} / P_{ITPA08} ratios in spherical tokamaks, which increasingly disagree with the ITER scaling as $A \to 1$ [26]. The power threshold has not yet been studied in a double null configuration, which may lead to $\sim 2\times$ decreases in P_{LH}.

Large and small ELMs are present in the H-mode phase. Their input power dependencies, measured magnetic toroidal mode number spectra, and field-aligned filament generation are consistent with observations in other high-performance devices. In conjunction with the modest edge parameters present at $A \sim 1$, highly resolved, unique measurements of nonlinear ELM dynamics are enabled on the Alfvénic timescales of the instability of import to validation of ELM models [49]. Measurements reported herein confirm the generation and expulsion of current-carrying filaments under the influence of large ELMs. However, differences are observed in the time duration of the ELM and the severity of their disturbance.

H-mode operations are found to be compatible with local helicity injection non-inductive startup [27], which conserves the limited Ohmic solenoid flux for subsequent plasma I_p sustainment. LHI employs compact, multi-megawatt edge current injectors located at the plasma boundary to inject DC magnetic helicity and thereby drive toroidal current without solenoid induction. Figure 20(a) shows I_p, helicity injector current I_{inj} and Ohmic loop voltage V_{loop} waveforms from a 170 kA LHI-initiated discharge using HFS fueling that transitions to Ohmic current drive and H-mode. An equilibrium reconstruction

during the H-mode phase (figure 20(b)) indicates the achievement of the highest stored energy plasmas produced in the device to date.

Leveraging the edge current injectors normally used for LHI, but at lower power, may afford a novel means of ELM modification through helical edge magnetic perturbations. Figure 21 shows initial investigations of the effects of injecting perturbing helical current streams with varied I_{inj} several cm outside the edge pedestal region along open field lines in the scrapeoff layer adjoining an H-mode plasma. This is conceptually similar to experiments conducted on EAST [50], where the helical edge current injection was established via RF current drive instead of helicity injectors. At relatively low $I_{inj} \lesssim 1$ kA, no effects on I_p or Φ_D are evident (figures 21(a) and (b)). However, a marked decrease in the small ELM activity occurs, as illustrated by reduced high-frequency D_α bursts in figures 21(c) and (d). For $I_{inj} > 2$ kA, a strong drop in I_p and Φ_D is evident as increasing perturbing field is applied, consistent with very strong perturbations of the edge and loss of H-mode confinement.

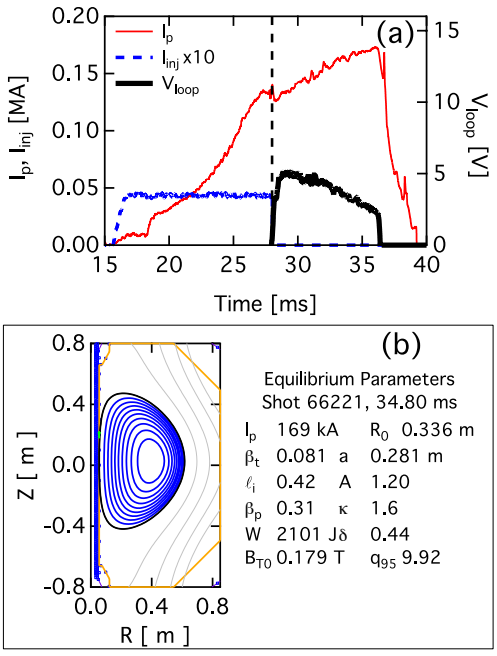

Figure 20. LHI startup to Ohmic H-mode. I_p (a) and H-mode equilibrium reconstruction (b).

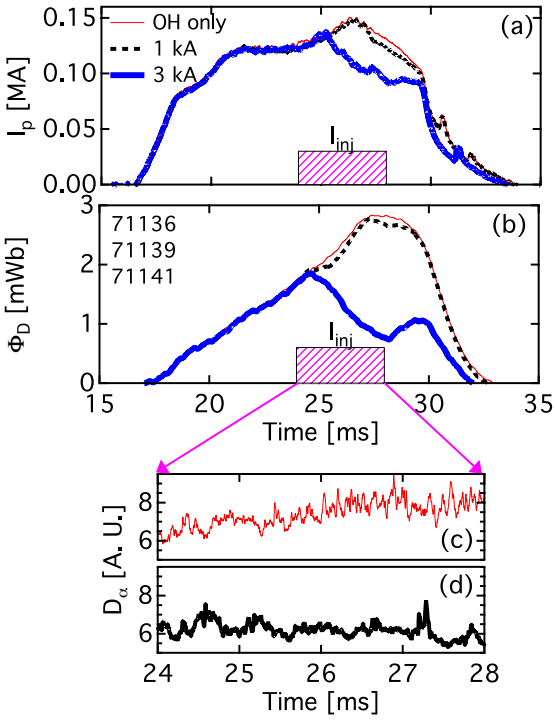

Figure 21. H-mode plasmas perturbed with helical current injection. I_p (a), Φ_D (b), and D_α emissions for OH only (c) and I_{inj} = 1 kA (d) cases.

Acknowledgments

The authors thank B.T. Lewicki, B.A. Kujak-Ford, and G.R. Winz for their technical assistance. This material is based upon work supported by the U.S. Department of Energy, Office of Science, Office of Fusion Energy Sciences, under Award Number DE-FG02-96ER54375. Data from this publication are publicly available in openly-documented, machine-readable formats [51]. Disclaimer: Any opinions, findings, and conclusions or recommendations expressed in this publication are those of the authors and do not necessarily reflect the views of the U.S. Department of Energy.

References

[1] Wagner F. *et al.* 1982 *Phys. Rev. Lett.* **49** 1408
[2] ITER Physics Basis Expert Groups on Confinement and Transport and Confinement Modelling and Database and ITER Physics Basis Editors 1999 *Nucl. Fusion* **39** 2175
[3] Leonard A.W. 2014 *Phys. Plasmas* **21** 090501
[4] Martin Y.R., Takizuka T. and the ITPA CDBM H-mode Threshold Data Group 2008 *J. Phys.: Conf. Ser.* **123** 012033
[5] Connor J.W. and Wilson H.R. 2000 *Plasma Phys. Control. Fusion* **42** R1
[6] Yan Z., McKee G.R., Fonck R., Gohil P., Groebner R.J. and Osborne T.H. 2014 *Phys. Rev. Lett.* **112** 125002
[7] Fundamenski W., Militello F., Moulton D. and McDonald D.C. 2012 *Nucl. Fusion* **52** 062003

[8] Lang P.T. *et al.* 2013 *Nucl. Fusion* **53** 043004
[9] Maingi R. *et al.* 2010 *Nucl. Fusion* **50** 064010
[10] Kaye S.M. *et al.* 2011 *Nucl. Fusion* **51** 113019
[11] Field A.R. *et al*. 2002 *Plasma Phys. Control. Fusion* **44** A113
[12] Takizuka T. and the ITPA H-Mode Database Working Group 2004 *Plasma Phys. Control. Fusion* **46** A227
[13] Meyer H. *et al*. 2006 *Nucl. Fusion* **46** 64
[14] Maingi R. *et al.* 2005 *Nucl. Fusion* **45** 1066
[15] Meyer H. *et al*. 2009 *Nucl. Fusion* **49** 104017
[16] Kass T., Günter S., Maraschek M., Suttrop W., Zohm H. and the ASDEX Upgrade Team 1998 *Nucl. Fusion* **38** 111
[17] Peng Y.K.M. and Strickler D.J. 1986 *Nucl. Fusion* **26** 769
[18] Battaglia D.J. *et al.* 2013 *Nucl. Fusion* **53** 113032
[19] Field A.R. and the MAST Team 2004 *Plasma Phys. Control. Fusion* **46** 981
[20] Maingi R. *et al.* 2004 *Plasma Phys. Control. Fusion* **46** A305
[21] Snyder P.B. *et al*. 2009 *Nucl. Fusion* **49** 085035
[22] Bongard M.W., Fonck R.J., Hegna C.C., Redd A.J. and Schlossberg D.J. 2011 *Phys. Rev. Lett.* **107** 035003
[23] Bongard M.W., Thome K.E., Barr J.L., Burke M.G., Fonck R.J., Hinson E.T., Redd A.J. and Schlossberg D.J. 2014 *Nucl. Fusion* **54** 114008
[24] Maingi R. *et al.* 2009 *Phys. Rev. Lett.* **103** 075001
[25] Garstka G.D. *et al.* 2006 *Nucl. Fusion* **46** S603
[26] Thome K.E., Bongard M.W., Barr J.L., Bodner G.M., Kriete D.M., Perry J.M. and Schlossberg D.J. 2016 *Phys. Rev. Lett.* **116** 175001
[27] Battaglia D.J., Bongard M.W., Fonck R.J. and Redd A.J. 2011 *Nucl. Fusion* **51** 073029
[28] Burke M.G., Fonck R.J., Bongard M.W., Schlossberg D.J. and Winz G.R. 2012 *Rev. Sci. Instrum.* **83** 10D516
[29] Sontag A.C., Fonck R.J., Garstka G.D., Unterberg E.A. and Thorson T.A. 2008 *Nucl. Fusion* **48** 095006
[30] Park J.-K., Bell R.E., Kaye S.M., Solomon W.M., LeBlanc B.P., Diallo A., Menard J.E., Kubota S. and the NSTX Research Team 2013 *Nucl. Fusion* **53** 063012
[31] Rice J.E. *et al*. 2011 *Phys*. *Rev. Lett.* **107** 265001
[32] Schlossberg D.J., Bongard M.W., Fonck R.J., Schoenbeck N.L. and Winz G.R. 2013 *J. Instrum.* **8** C11019
[33] Selden A.C. 1980 *Phys. Lett. A* **79** 405
[34] Sykes A. *et al.* 1997 *Plasma. Phys. Control. Fusion* **39** B247
[35] Thome K.E., Bongard M.W., Burke M.G., Dowd A.S., Fonck R.J., Redd A.J. and Schlossberg D.J. 2011 *Bull. Am. Phys. Soc.* **56** PP9.6 (http://meetings.aps.org/link/BAPS.2011.DPP.PP9.6)
[36] Bongard M.W., Fonck R.J., Lewicki B.T. and Redd A.J. 2010 *Rev. Sci. Instrum.* **81** 10E105
[37] Petty C.C., Fox W.R., Luce T.C., Makowski M.A., and Suzuki T. 2002 *Nucl. Fusion* **42** 1124
[38] Garstka G.D., Diem S.J., Fonck R.J., Lewicki B.T., Sontag A.C., Tritz K.L. and Unterberg E.A. 2003 *Phys. Plasmas* **10** 1705
[39] Groebner R.J. and Carlstrom T.N. 1998 *Plasma Phys. Control. Fusion* 40 673
[40] Ma Y., Hughes J.W., Hubbard A.E., LaBombard B., Churchill R.M., Golfinopolous T., Tsujii N. and Marmar E.S. 2012 *Nucl. Fusion* **52** 023010
[41] Burrell K.H. *et al*. 1989 *Plasma Phys. Control. Fusion* **31** 1649
[42] Carlstrom T.N., Shimada M., Burrell K.H., DeBoo J., Gohil P., Groebner R., Hsieh C., Matsumoto H. and Trost P. 1989 *Proc. 16th EPS Conf. on Controlled Fusion Plasma Physics Europhysics Conf. Abstracts* vol 13B (*Venice: 13-17 March 1989*) p 241
[43] Kirk A., Koch B., Scannell R., Wilson H.R., Counsell G., Dowling J., Herrmann A., Martin R.,

Walsh M. and the MAST Team 2006 *Phys. Rev. Lett.* **96** 185001
[44] Zohm H. 1996 *Plasma Phys. Control. Fusion* **38** 105
[45] Sugiyama L.E. 2015 *Nucl. Fusion* **55** 073006
[46] Snyder P.B., Wilson H.R. and Xu X.Q. 2005 *Phys. Plasmas* **12** 056115
[47] Pamela S.J.P., Huysmans G.T.A., Beurskens M.N.A., Devaux S., Eich T., Benkadda S. and JET EFDA Contributors 2011 *Plasma Phys. Control. Fusion* **53** 054014
[48] Myra J.R. 2007 *Phys. Plasmas* **14** 102314
[49] Huijsmans G.T., Chang C.S., Ferraro N., Sugiyama L., Waelbroeck F., Xu X.Q., Loarte A., and Futatani S. 2015 *Phys. Plasmas* **22** 021805
[50] Liang Y. *et al.* 2013 *Phys. Rev. Lett.* **110** 235002
[51] Thome K.E., Bongard M.W., Barr J.L., Bodner G.M., Burke M.G., Fonck R.J., Kriete D.M., Perry J.M., Reusch J.A. and Schlossberg D.J., 2016 Public Data Set: H-mode plasmas at very low aspect ratio on the Pegasus Toroidal Experiment (online) (doi:10.18138/1236495)